
Comparison of 2-Dimensional and 3-Dimensional Acquisition for ^{18}F -FDG PET Oncology Studies Performed on an LSO-Based Scanner

Martin A. Lodge, PhD¹; Ramsey D. Badawi, PhD²; Richard Gilbert, AA³; Pablo E. Dibos, MD⁴; and Bruce R. Line, MD¹

¹Division of Nuclear Medicine, Department of Radiology, University of Maryland Medical School, Baltimore, Maryland; ²Department of Radiology, University of California Davis Medical Center, Sacramento, California; ³PET/CT Imaging at White Marsh, Nottingham, Maryland; and ⁴Division of Nuclear Medicine, Good Samaritan Hospital, Baltimore, Maryland

Three-dimensional (3D) PET acquisition has the potential to reduce image noise but the advantage of 3D PET for studies outside the brain has not been well established. To compare the performance of 2-dimensional (2D) and 3D acquisition for whole-body ^{18}F -FDG applications, a series of patient studies were performed using a lutetium oxyorthosilicate (LSO)-based tomograph. **Methods:** Comparative 2D and 3D images were acquired for 27 oncology patients using an LSO-based tomograph. Data acquisition (350–650 keV, 6 ns) started 99 ± 12 min (mean \pm SD) after injection of 624 ± 76 MBq ^{18}F -FDG. Bias caused by tracer redistribution and decay was eliminated by acquiring dynamic data over a single-bed position using a protocol that alternated between septa-in and septa-out modes (2D, 3D, 2D, 3D, 2D, 3D). Frames were combined to form 8 statistically independent sinograms: four 2D replicates (105 s) and four 3D replicates (90 s). The different frame durations in 2D and 3D compensated for the different number of overlapping bed positions required for an 85-cm whole-body study. Images were reconstructed with either 2D or fully 3D ordered-subsets expectation maximization (2 iterations and 8 subsets; 2D 6-mm gaussian, 3D 5- and 6-mm gaussian). Image target-to-background ratio was assessed by dividing the lesion maximum by the mean within a neighboring background region. Image noise was assessed by applying background regions of interest to the replicate images and calculating the within-patient coefficient of variation. **Results:** The difference in target-to-background ratio between the 2D and 3D images, when they were filtered with 6-mm and 5-mm gaussian filters, respectively, was not highly statistically significant ($P = 0.16$). The mean ratio of 3D to 2D image values was 0.94 with 95% limits of agreement of 0.63–1.41. The within-patient coefficients of variation for the 2D and 3D images were $13\% \pm 15\%$ and $9\% \pm 10\%$, respectively ($P = 0.0005$). **Conclusion:** Under conditions of matched target to-to-background ratios, the 3D mode was found to produce images with significantly less variability than the 2D mode. These data provide support for the use of 3D acquisition with LSO detectors to reduce scan times in whole-body ^{18}F -FDG applications.

Key Words: PET; 2D; 3D; LSO; acquisition

J Nucl Med 2006; 47:23–31

Whole-body PET using the glucose analog ^{18}F -FDG has proven to be highly valuable in many oncology applications (1) despite the fact that image quality is frequently limited by statistical noise. As in other PET applications, high noise can be attributed to the relatively low sensitivity of clinical scanners and the limited levels of radioactivity that can be administered to patients because of radiation safety and scanner counting rate considerations. In whole-body applications the issue is compounded by the need for extended axial coverage and, to produce images of sufficient statistical quality, data acquisition periods can be lengthy. Reducing the length of the scanning procedure would clearly improve patient comfort, reduce the likelihood of patient motion, and also increase patient throughput. However, unless otherwise compensated, shorter data acquisition periods would lead to increasingly noisy images that may compromise accurate interpretation.

One of the factors that has limited the sensitivity of many PET tomographs is the presence of interplane septa. Current scanners, particularly those based on bismuth germanate (BGO) scintillation crystals, have limited energy resolution meaning that scattered photons cannot be completely rejected by energy discrimination. To reduce the number of scattered photons that reach the detectors, annular septa are positioned so as to absorb photons incident at large oblique angles. These septa effectively reduce the proportion of scattered photons that are measured but they also reduce the sensitivity for unscattered photons. Whereas in single-photon γ -camera imaging the collimator is essential for image formation, in PET the septa are not necessary to provide positional information and data acquisition can be performed in either septa-in or septa-out modes. Both modes of operation result in 3-dimensional (3D) volumetric

Received Jul. 7, 2005; revision accepted Sep. 21, 2005.
For correspondence contact: Martin A. Lodge, PhD, Division of Nuclear Medicine, University of Maryland Medical Center, 22 South Greene St., Baltimore, MD 21201.
E-mail: mlodge@umm.edu

images, but data acquisition with the septa in the field of view has been referred to as the 2-dimensional (2D) mode and data acquisition with no septa has been referred to as the 3D mode.

The higher sensitivity of 3D acquisition would seem to give it a clear noise advantage over 2D acquisition, but the issue is complicated by several factors (2). Removing the septa increases sensitivity by a factor of around 5–7 (3,4), resulting in much higher counting rates. This is, of course, the objective of 3D acquisition but the higher counting rates can also lead to greater detector dead time, which may mean that the expected increase in system sensitivity is not fully realized in clinical practice. Furthermore, increased counting rates for true coincidence events are associated with even greater increases in counting rates for random coincidences. Whereas trues (ideally) increase linearly with activity in the field of view, randoms increase with the square of activity (5) and can rapidly overtake the trues rate. Randoms correction can be implemented by acquiring additional data in a delayed time window, but compensating for a large randoms component can increase noise and further reduces the potential performance advantage of the 3D mode. Scatter is also an important issue because part of the increased sensitivity obtained in 3D is due to the detection of a large number of unwanted scattered photons. Scatter fractions of 10%–20% that have been reported for 2D acquisition increase to 40%–50% in 3D and may still underestimate the situation encountered in clinical body applications (6). When these issues are considered the advantage of 3D acquisition is not at all obvious.

Evaluating the relative performance of 2D and 3D acquisition is itself a complicated task because of the large number of variables that may influence the comparison. 3D performance is expected to be application dependent as the extent of the dead time, randoms, and scatter issues is likely to be different for different clinical situations. In addition, results may vary depending on the tasks and metrics used for image quality assessment and conflicting reports can be found in the literature. Cherry et al. (7) have shown that 3D acquisition can lead to greater signal-to-noise ratios and improved detection of local changes in cerebral blood. Badawi et al. (6) found that improved noise-equivalent counting rate performance was obtained in 3D for a range of object sizes and activity concentrations, including those applicable to whole-body imaging situations. However, comparisons of 2D and 3D performance in high counting rate, high-scatter ^{82}Rb cardiac studies have shown either a disadvantage for 3D (8) or images of comparable quality (9). In ^{18}F -FDG whole-body applications important work has been done comparing lesion detection using phantoms and simulated data. Raylman et al. (10) found no statistically significant difference in lesion detection between 2D and 3D and Lartizien et al. (11) found an advantage for 3D only when the administered activity was optimized for 3D. Farquhar et al. (12) and Lodge et al. (13) compared 2D and 3D acquisition using clinical data and found no

advantage for 3D in terms of lesion detection or image noise, whereas El Fakhri et al. (14) found an advantage for 3D in terms of lesion detection but only for smaller patients and low-activity concentrations.

A possible cause of the poor 3D performance that has been reported for body applications is that all the above studies were performed on BGO-based tomographs that were not optimized for 3D. Scanners with detectors based on crystals such as gadolinium oxyorthosilicate (GSO) (15) and lutetium oxyorthosilicate (LSO) (16) may give more favorable 3D results because of reduced randoms and dead time and potentially improved scatter rejection. The present study was performed on the ECAT Accel (CPS Innovations), which is the first production clinical PET scanner with LSO crystals and is one of the few non-BGO scanners that is capable of both 2D and 3D acquisition. To compare the 2 acquisition modes under realistic conditions, we used patient data and minimized effects that could bias the outcome. The effects of tracer redistribution and isotope decay between 2D and 3D acquisitions were minimized by using a protocol that alternated between septa-in and septa-out acquisitions. 2D and 3D images were reconstructed using the same ordered-subsets expectation maximization (OSEM) algorithm in 2D and fully 3D forms. In addition, care was taken to compare image noise under conditions of matched lesion contrast. Specifically, lesion target-to-background ratios were matched in both the 2D and 3D patient images, which included scatter and other effects that could lead to poorer lesion contrast than that expected from in-air phantom measurements.

Although the main advantage of 3D acquisition is improved sensitivity, there are other benefits that are related to scanner design. These include the potential to enlarge the patient port by eliminating the septa, allowing improved patient access and reduced production costs. In terms of image quality, however, the main advantage that has been proposed for 3D acquisition is increased sensitivity. It is expected that (all other things being equal) any increase in sensitivity will translate to reduced image noise and potentially improved lesion detection or, alternatively, to shorter acquisitions that produce images of similar quality. The aim of this study was to determine whether image noise in whole-body ^{18}F -FDG applications was, in fact, reduced with 3D acquisition when similar reconstruction algorithms were used to produce images of similar contrast to those obtained in 2D. Without such a reduction there would seem to be no possibility for improved lesion detection and no scope for reduced scan times without compromising image quality.

MATERIALS AND METHODS

Patient Population

The study population consisted of patients who had whole-body ^{18}F -FDG PET studies as part of their clinical management. After completion of the whole-body scans, 27 patients (20 male, 7 female) volunteered for additional research acquisitions. The mean patient

weight was 87 ± 18 kg and ranged from 59 to 118 kg. The mean body mass index (weight divided by height squared) was 28.3 ± 4.9 and ranged from 19.8 to 38.8. Research data acquisition was approved by the appropriate Institutional Review Board and is described below. All research data were anonymous from the outset and the clinical whole-body images did not form part of the study.

PET Tomograph

All image data were acquired on an ECAT Accel PET scanner. This scanner consisted of 9,216 LSO crystals that were arranged in a block design. Individual detector blocks contained 64 crystals, each with dimensions $6.45 \times 6.45 \times 25$ mm. The axial and transaxial field of view was 162 mm and 585 mm, respectively. Interplane septa could be moved in and out of the field of view to allow either 2D or 3D data acquisition. The transverse spatial resolution (17) of the system for 3D acquisition was 6.1-mm full width at half maximum (FWHM) at the center and 6.7-mm FWHM at a radius of 10 cm. For 2D acquisition the same parameters were 6.1 and 6.8 mm. The axial resolution was 4.5 mm for 3D and 4.6 mm for 2D at the center of the field of view. Data were acquired using a 350- to 650-keV energy window and a 6-ns coincidence timing window. Transmission data were measured using three $^{68}\text{Ga}/^{68}\text{Ge}$ positron sources that operated with the septa in the field of view.

Acquisition Protocol

All patients fasted for 4 h before an ^{18}F -FDG administration of 7.48 ± 1.67 MBq/kg. The mean amount of activity was 624 ± 76 MBq (16.9 ± 2.1 mCi) and the mean time between injection and the start of the research acquisition was 99 ± 12 min. Image data were acquired over a single-bed position and, wherever possible, included an area of suspected disease. The single-bed position research acquisitions were acquired over the neck ($n = 1$), upper chest ($n = 8$), lower chest ($n = 9$), and abdomen ($n = 9$). Twenty-five patients were scanned with arms by their sides in the field of view and 2 patients were scanned with arms out of the field of view.

To reduce bias caused by radioactive decay and tracer redistribution, data were obtained using a protocol that alternated between 2D and 3D in an interleaved fashion (Fig. 1). At each position of the septa a short dynamic emission scan was acquired and the resulting sequence of imaging was as follows: 4×35 s 2D, 4×30 s 3D, 4×35 s 2D, 4×30 s 3D, 4×35 s 2D, and 4×30 s 3D. The total time for this protocol was 24 min and included

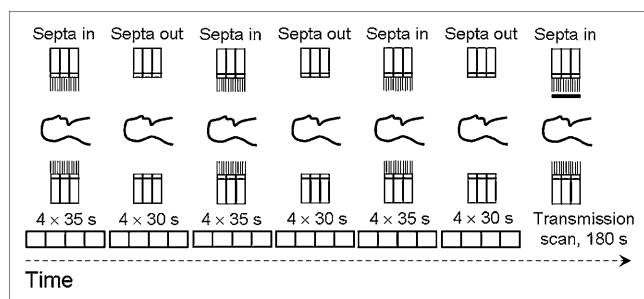


FIGURE 1. Research data acquisition occurred over a single-bed position using an interleaved septa-in/septa-out acquisition protocol. At each position of the septa, emission data were acquired in a dynamic mode (4 frames of either 30- or 35-s duration). Six dynamic emission scans were acquired followed by a 3-min transmission scan.

approximately 1 min to move the septa and configure data acquisition before each scan. Upon completion of the final scan the data were combined to form 4 separate 2D sinograms and 4 separate 3D sinograms. For each acquisition mode the corresponding frames from each of the 3 dynamic scans were summed to form composite sinograms. In this way 4 statistically independent 2D sinograms (4×105 s) and 4 statistically independent 3D sinograms (4×90 s) were formed. Because the composite sinograms in both 2D and 3D modes were made up from multiple shorter datasets acquired over a similar period, the effective time difference between the 2D and 3D data was minimized. In addition to the independent replicate sinograms described, 2 additional sinograms were produced by summing all data in each mode to form low-noise 2D (420 s) and 3D (360 s) sinograms.

The reason that the 2D acquisitions were performed for multiples of 35 s and the 3D acquisitions were performed for multiples of 30 s is related to the required bed overlap for multibed studies. Because of the different axial sensitivity profiles in 2D and 3D, the 2 acquisition modes require different bed overlaps to ensure approximately uniform sensitivity. In 2D the Accel requires a 5-plane overlap (16.9 mm), whereas in 3D it requires an 11-plane overlap (37.1 mm). Although data were only acquired over a single-bed position, the intention was to reproduce the noise typical of an 85-cm multibed study. Axial coverage of 85 cm requires 6 bed positions in 2D but 7 bed positions in 3D. For this reason comparable scan times in 3D were a factor of 6/7 that in 2D.

Before the summation described above, all sinograms were corrected for random coincidence events using online subtraction of data collected in a delayed window. A 3-min $^{68}\text{Ga}/^{68}\text{Ge}$ transmission scan was acquired immediately after each patient's final emission acquisition and used for attenuation correction. The transmission data were segmented (18) according to our standard clinical protocol, and the resulting attenuation correction factors were applied to all 2D and 3D emission data. Scatter correction was applied to both the 2D (scatter deconvolution (19)) and the 3D (model-based scatter simulation (20)) data before image reconstruction using the attenuation-weighted OSEM algorithm (21). The standard clinical implementation was used for the 2D reconstructions and a "fully 3D" implementation (22) was used for the 3D data. The 3D algorithm directly reconstructed the 3D image volume without rebinning the projection data into transverse sinograms. Both 2D and 3D sinograms had 192 elements \times 192 views and were reconstructed into a 128×128 matrix with a voxel size of $0.514 \times 0.514 \times 0.338$ cm. All data were corrected for attenuation and normalization before image reconstruction but both 2D and 3D OSEM included attenuation weighting, which ensured that each line of response was approximately weighted according to its variance. All reconstructions used 2 iterations and 8 subsets, which were the manufacturer's recommended settings for clinical whole-body studies. After reconstruction, noise was reduced by smoothing the images with a 6-mm FWHM gaussian filter. Additional 3D images were reconstructed with a 5-mm gaussian filter.

Image Analysis

Region-of-interest (ROI) analysis was used to quantify lesion target-to-background ratios and image noise. For each patient a series of ROIs were defined on the 420-s 2D image. As the interleaved data acquisition protocol ensured almost perfect spatial registration of all images acquired on the same patient,

these ROIs were applied to all images for that patient without the need for further manipulation. Lesion target-to-background ratio was measured by calculating the maximum pixel value in a small elliptical ROI placed over a lesion and dividing by the mean value within a second ROI placed in a background region (Fig. 2). To minimize the effect of noise on the measurement of the lesion maximum we used the low-noise (420-s 2D, 360-s 3D) images for the analysis of target-to-background ratio. For the noise analysis only the 3D images with the 5-mm gaussian smooth were considered. Image noise was measured by defining a 1.5-cm square ROI in a background region of the central slice. Applying this ROI to the replicate images produced 4 statistically independent measurements of local activity concentration for both 2D (C_i^{2D} , where $i = 1, 2, 3, 4$) and 3D (C_i^{3D} , where $i = 1, 2, 3, 4$) modes. The variability of these measurements was analyzed using the method described below to estimate image noise.

Statistical Analysis

Statistical analysis was performed according to the method of Bland and Altman (23–25), which is summarized here. Before performing this analysis, the target-to-background ratios in the 2D and 3D images were compared to confirm that they were matched. Because of the natural pairing of the data, a paired Student t test was used to assess the significance of differences between the 2D and 3D target-to-background ratios.

Under the assumption of matched target-to-background ratios between the 2D and 3D images, these data were compared in terms of quantitative agreement and variability. For each patient and acquisition mode the mean (m_{2D} and m_{3D}) of the 4 replicate background ROI values (C_i^{2D} and C_i^{3D}) was determined. Agreement of the 2D and 3D data was measured by calculating, for each patient, the difference d between the mean ROI data for the 2 modes:

$$d = m_{3D} - m_{2D}.$$

Any dependence between d and the magnitude of the underlying data was determined by plotting d against a , the average of m_{2D} and m_{3D} :

$$a = 0.5 \times (m_{2D} + m_{3D})$$

and tested using a rank correlation coefficient (Kendall τ). In the event of a significant correlation, the data were logarithmically

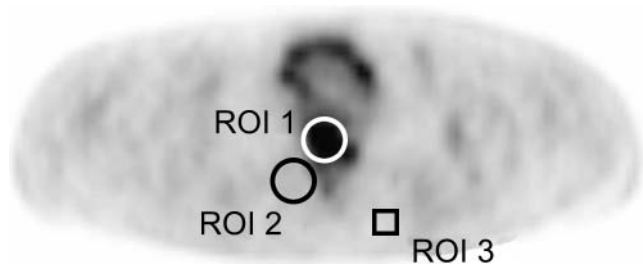


FIGURE 2. Lesion contrast was estimated by dividing the maximum pixel value in a target region (ROI 1), by the mean pixel value in a background region (ROI 2). Image noise was estimated by placing a 1.5 × 1.5 cm square region (ROI 3) in a background area of the central slice. Note that in this example the lesion was present in the central slice, although this was not typically the case.

transformed (base 10) and the analysis repeated. Logarithmic transformation is effective at removing the proportionality between parameters of this kind. Failure to eliminate this dependence would mean that the limits of agreement would be overestimated for regions of low activity and underestimated for regions of high activity. The mean (D) and the standard deviation (s) of d was calculated for all patients. D represents the mean difference between 2D and 3D and the 95% limits of agreement were determined from $D \pm 1.96 s$. These limits represent the values between which 95% of differences lie under the assumption that d is normally distributed (Shapiro–Wilk test). Results on the logarithmic scale were transformed back to the original units by taking the inverse logarithm.

Image noise was calculated for each acquisition mode as follows. For each patient the SD of the 4 replicate ROI values were plotted as a function of their mean. Similar to the above analysis, any proportionality between the SD and the mean was tested using the Kendall τ . In the event of a significant dependence, the ROI data values were logarithmically transformed and the above analysis was repeated. The within-subject SD was determined by averaging the variances (square of the SD) for each patient and taking the square root. This is the within-subject SD on a logarithmic scale, which can be converted to the within-subject coefficient of variation in the original units by taking the inverse logarithm and subtracting 1. The within-subject coefficient of variation is the ratio of SD to the mean and was the parameter used to quantify image noise in this study. The significance of differences between 2D and 3D noise was determined by comparing the variances using a paired t test.

RESULTS

The mean dimensions of all lesions, estimated from the PET images, were 2.2 ± 0.9 cm × 2.6 ± 1.3 cm × 2.8 ± 1.1 cm. Figure 3A shows data for lesion target-to-background ratio in both 2D and 3D images when both sets of images were smoothed with a 6-mm FWHM gaussian filter. There is a statistically significant difference ($P = 0.005$) between the 2 modes of acquisition with 2D having an average target-to-background ratio of 6.0 ± 3.3 and 3D having a ratio of 5.5 ± 2.8 . The mean ratio of 3D to 2D target-to-background ratio was 0.95 ± 0.12 , indicating a superior target-to-background ratio in 2D mode. Figure 3B shows data similar to that of Figure 3A except, in this case, the 3D images were smoothed with a 5-mm gaussian filter. The mean target-to-background ratio is now 6.0 ± 3.3 for 2D and 5.8 ± 3.0 for 3D with no highly statistically significant difference ($P = 0.16$) between the 2. The mean ratio of 3D to 2D target-to-background ratio was 1.00 ± 0.12 , indicating that the 2 acquisition modes gave rise to images with approximately equal lesion contrast.

Figure 4A shows the difference, d , between the corresponding 2D (6-mm gaussian) and 3D (5-mm gaussian) data as a function of their average, a . The Kendall τ was -0.248 ($P = 0.07$), indicating that d was not proportional to a at the 0.05 level of significance. However, proportionality could not be ruled out (Fig. 4A) and the data were logarithmically transformed. Figure 4B shows the data on a logarithmic scale where there is no evidence

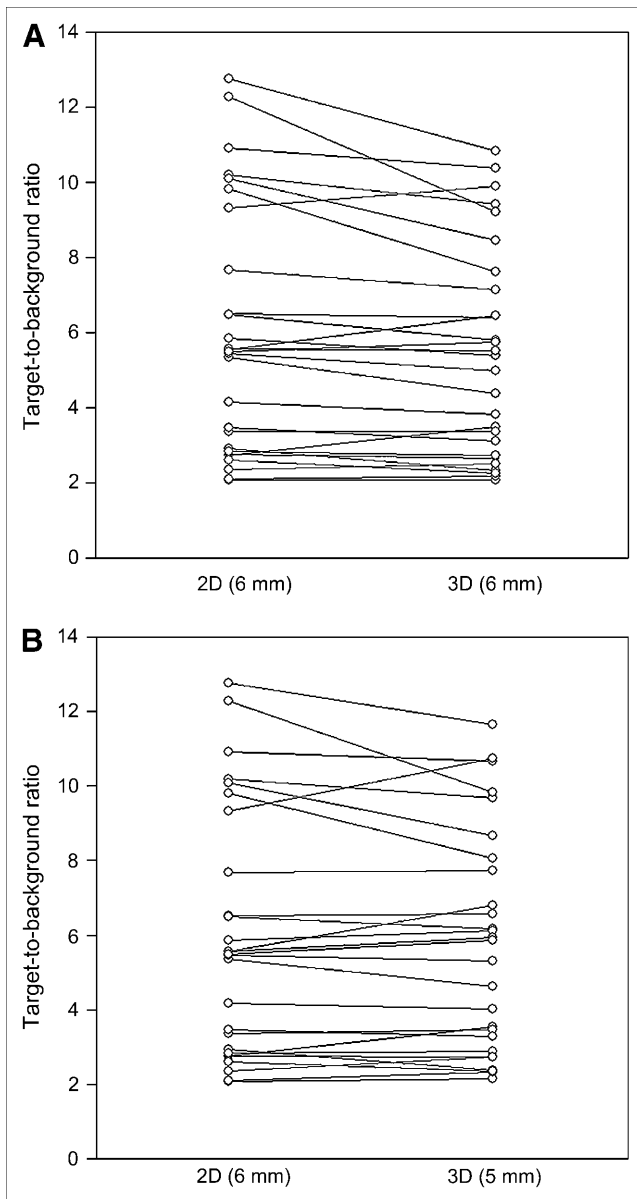


FIGURE 3. Target-to-background ratios for the 420-s 2D and 360-s 3D images. (A) Both 2D and 3D images were smoothed with a 6-mm FWHM gaussian filter after OSEM reconstruction. Mean target-to-background ratios for 2D and 3D images were 6.0 ± 3.3 and 5.5 ± 2.8 ($P = 0.005$), respectively. (B) 2D images were smoothed with a 6-mm FWHM gaussian filter; and 3D images were smoothed with a 5-mm gaussian filter. Mean target-to-background ratios for 2D and 3D images were 6.0 ± 3.3 and 5.8 ± 3.0 ($P = 0.16$), respectively.

for proportionality (Kendall $\tau = -0.151$; $P = 0.27$). On this scale the mean difference D between the 2D and 3D data was -0.027 and the 95% limits of agreement were -0.202 and 0.148 . Converting these data back to the original units results in a mean relative difference of 0.94 with 95% limits of agreement of 0.63 – 1.41 . In other words, 3D acquisition produced concentration estimates that were lower than 2D by, on average, 6%.

Figure 5A examines the repeatability of the 2D data (6-mm gaussian) and shows a plot of the SD of C_i^{2D} as a function of its average. The magnitude of the SD was proportional to the average (Kendall $\tau = 0.345$; $P = 0.012$) so the data were logarithmically transformed. After logarithmic transformation (Fig. 5B) there was no evidence for proportionality (Kendall $\tau = -0.094$; $P = 0.491$). The within-subject SD (square root of the mean of the variances) was 0.054 on the logarithmic scale. After inverse logarithmic transformation and subtracting 1, the within-subject coefficient of variation was 0.13 ± 0.15 .

Figures 6A and 6B show the corresponding data for the 3D (5-mm gaussian) images. As for the 2D data, Figure 6A shows that the SD was proportional to the average (Kendall $\tau = 0.328$; $P = 0.017$). After logarithmic transformation (Fig. 6B) there was no evidence of proportionality (Kendall $\tau = -0.020$; $P = 0.884$) and the within-subject SD was 0.037 . After inverse logarithmic transformation and subtracting 1, the within-subject coefficient of variation was 0.09 ± 0.10 .

A paired t test confirmed that the difference between the 2D and 3D variance data, and thus the within-subject

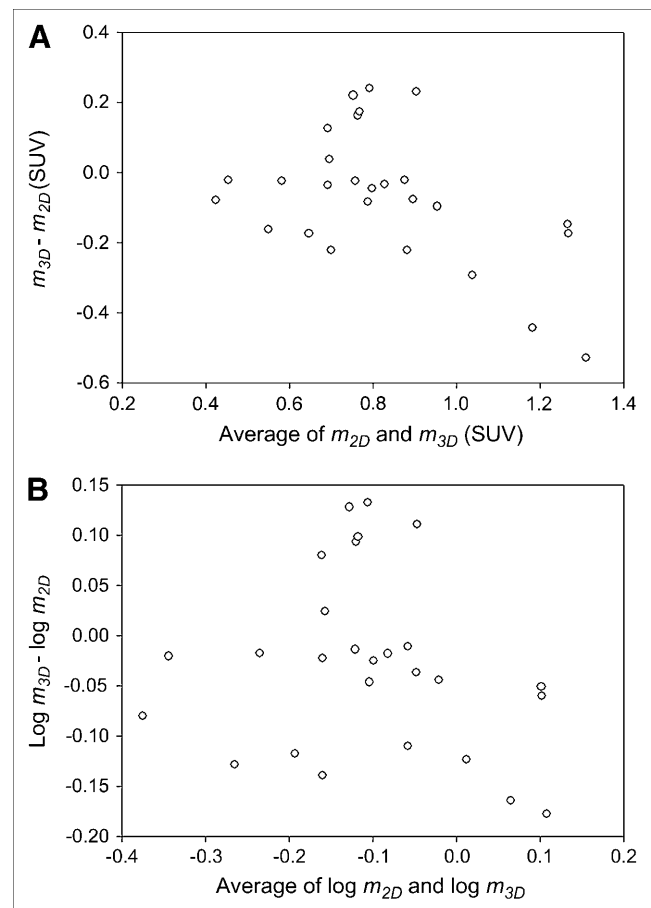


FIGURE 4. Difference between 2D and 3D measurements, d , as a function of the average of the 2D and 3D measurements, a . (A) Data are shown in original units (SUV = standardized uptake value). (B) Data are shown after logarithmic transformation.

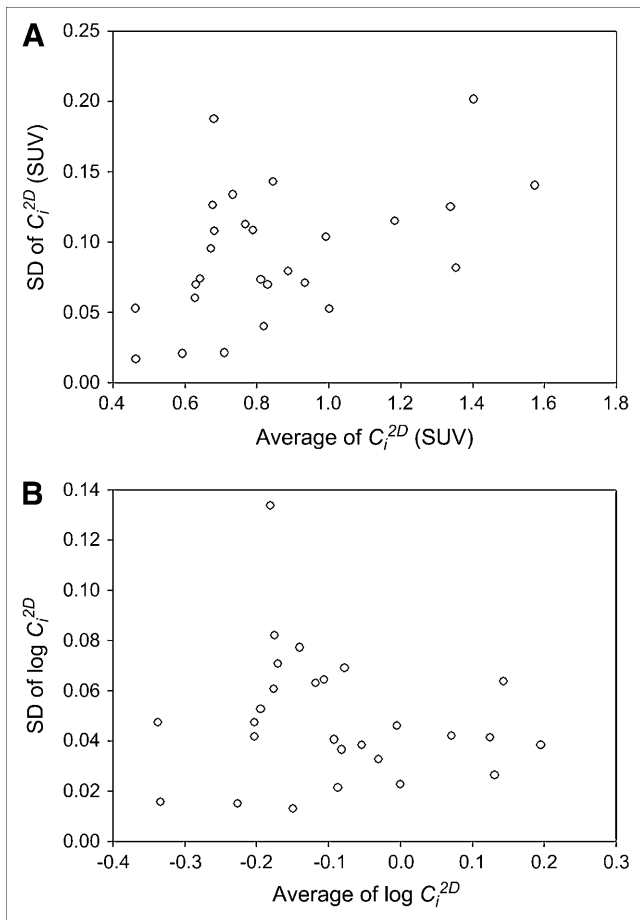


FIGURE 5. SD of 2D ROI data C_i^{2D} as a function of their average. (A) Data are shown in original units (SUV = standardized uptake value). (B) Data are shown after logarithmic transformation.

coefficient of variation, was highly significant ($P = 0.0005$). This result was supported by visual inspection of corresponding images (Fig. 7), which showed lower image noise in the case of 3D acquisition.

DISCUSSION

The main advantage of the current acquisition protocol was that it allowed comparative data to be acquired in real patients as opposed to phantoms and, thus, included all of the effects that influence clinical scans. By scanning over a single-bed position using an interleaved protocol, the 2D and 3D data were effectively acquired at very similar points in time (average time difference = 3.5 min). Differences in tracer concentration due to redistribution and radioactive decay were thus almost entirely eliminated. In addition, bias caused by patient motion at any stage in the acquisition was minimized as motion will have a similar effect on both the 2D and 3D images when acquired in an interleaved mode. This is because each replicate image was itself made from 3 shorter sinograms that were acquired at different times during the total acquisition period. Motion may have

caused a loss of resolution in both 2D and 3D images but no spatial misregistration was observed. The fact that the 2D and 3D images were inherently registered meant that ROIs could be applied to identical points in each image, reducing bias caused by software registration or manual repositioning of regions.

The within-patient coefficients of variation for 2D and 3D acquisition measured from our replicate data confirmed the visual impression (Fig. 7) that the 3D images were less noisy. The effect that this may have on lesion detection was not addressed in this study but it does provide some support for a reduction in scan duration with 3D acquisition and LSO detectors. 2D and 3D coefficients of variation (COV_{2D} and COV_{3D}) of 0.13 ± 0.15 and 0.09 ± 0.10 mean that, for equal scan durations, $COV_{3D} = 0.69 COV_{2D}$. Riddell et al. (26) have shown that for OSEM, the coefficient of variation is inversely proportional to the square root of the number of detected annihilation events (and therefore to scan duration for durations that are small compared with the radionuclide half-life). Making this assumption for our data, 3D scan durations can be reduced by a factor of ~ 0.48 (0.69^2) compared with the corresponding 2D acquisitions

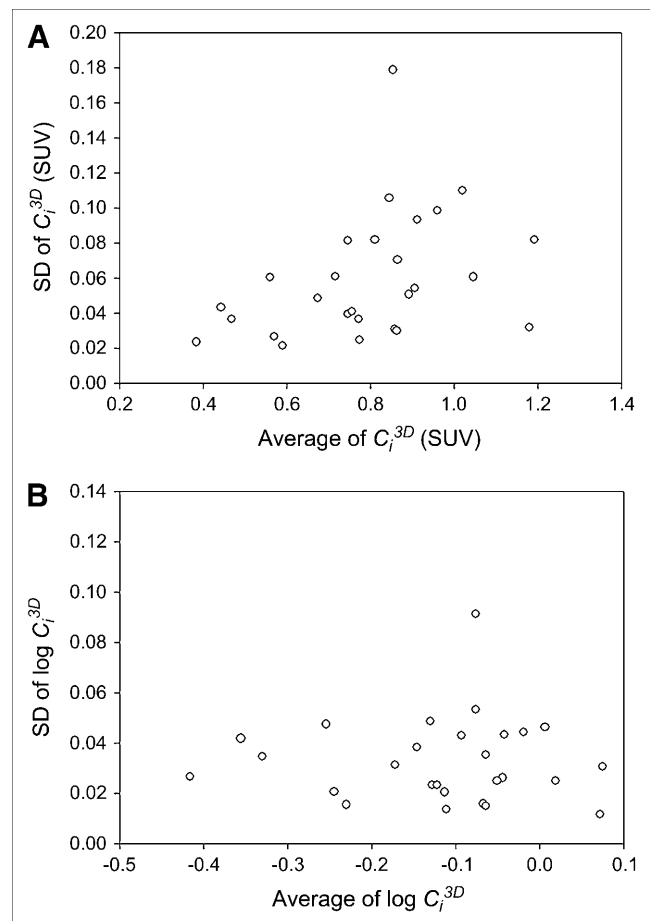


FIGURE 6. SD of 3D ROI data C_i^{3D} as a function of their average. (A) Data are shown in original units (SUV = standardized uptake value). (B) Data are shown after logarithmic transformation.

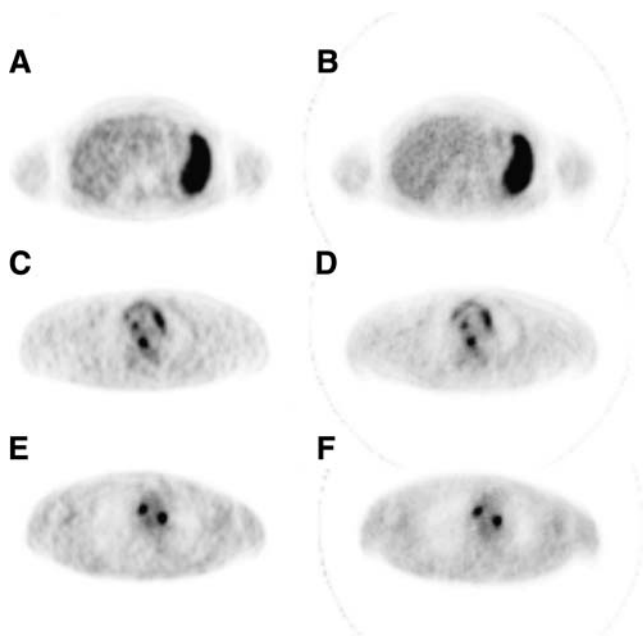


FIGURE 7. Example images from 3 patient studies. Images A, C, and E were acquired in 2D (105 s, 6-mm gaussian); images B, D, and F are the corresponding image slices acquired in 3D (90 s, 5-mm gaussian). The lower coefficient of variation in the 3D images can be perceived in images B, D, and F.

without degrading image noise. Note that these coefficients of variation reflect image noise and not the reproducibility of the technique as the replicate images were acquired after a single ^{18}F -FDG administration.

Although the interleaved acquisition protocol had the advantage that it allowed 2D and 3D data to be acquired under the same physiologic conditions, it had the disadvantage that—since the counting rate performance of the 2 acquisition modes was different—both 2D and 3D acquisitions could not be simultaneously optimized. In the present study, emission data were acquired around 100–120 min after tracer administration, whereas typical 2D whole-body scans are performed around 60–110 min after injection. The current research protocol therefore accurately reflects the counting rates that might be encountered toward the end of a 2D whole-body scan but does not represent the situation at earlier times. At earlier, more typical whole-body scan times, 3D image noise may be worse than at the late time point measured in the present study because of increased randoms and dead time. However, identical 3D noise performance can be achieved at the earlier scan time, simply by reducing the administered activity to compensate for the shorter decay time. 2D noise performance will not be degraded significantly by the higher counting rates encountered 60 min after injection and image noise will improve because of the higher number of detected photons. We can estimate the improvement in 2D image noise based on the average activity in the field of view during a typical 2D whole-body scan and during our experimental protocol. Assuming no tracer redistribution,

the average activity in the field of view A_{mean} between time t_1 and t_2 is given by:

$$A_{mean} = \frac{A_0}{(t_2 - t_1)} \int_{t_1}^{t_2} \exp(-\ln(2)t/t_{1/2}) dt,$$

where A_0 is proportional to the injected activity and $t_{1/2}$ is the physical half-life of the radioisotope (110 min). A_{mean} can be calculated for a typical 2D whole-body scan lasting 50 min and starting 60 min after tracer administration and also for the current research protocol, which involved a 20-min emission acquisition period, starting 100 min after tracer administration. On this basis, the mean activity for the typical 2D scan starting at 60 min is greater than the current research protocol by a factor of 1.17. The advantage in terms of shorter 3D scan times, which was previously calculated around 100 min after injection, should therefore be reduced by a factor of not more than 1.17.

Furthermore, in the present study, both 2D and 3D data were acquired after an average ^{18}F -FDG administration of 7.48 ± 1.67 MBq/kg. This is consistent with the recommendations of the manufacturer for 3D acquisition and similar to those suggested by Everaert et al. (27), who found a dose of 8 MBq/kg or greater to give best results. However, our mean injected activity of 624 ± 76 MBq (16.9 ± 2.1 mCi) was less than the amount that is sometimes given for 2D acquisition, which may be as high as 740 MBq (20 mCi). Increasing the administered activity in 2D from 624 MBq to 740 MBq, assuming detector dead time and other issues remain the same, would mean that the advantage of 3D in terms of shorter scan durations would be reduced by a factor of 1.19 ($740 \text{ MBq}/624 \text{ MBq}$). In other words, scans acquired in 3D on this LSO scanner can be shorter by a factor of 0.67 ($0.48 \times 1.17 \times 1.19$) compared with those acquired in 2D for similar noise quality.

The metric used for noise evaluation, the within-subject coefficient of variation, is the parameter recommended for evaluations of this sort (25) as it reflects the within-patient SD as a function of the mean of the data. It is therefore not susceptible to systematic differences such as errors in the calibration of the scanners in 2D and 3D modes. However, it may be influenced by other effects, such as differences in the accuracy of the 2D and 3D scatter corrections. The 3D image data were, on average, lower than corresponding 2D data by 6% (Fig. 4). This difference may be due to errors in scanner calibration or it may be a result of the 3D scatter correction overcorrecting the 3D data compared with the corresponding 2D correction. The latter would tend to reduce the mean image value, leading to an overestimation of the coefficient of variation in 3D. We therefore do not believe that the lower coefficient of variation observed in 3D is a consequence of the small difference in the mean 2D and 3D image values.

The small differences in target-to-background ratios that were observed when identical smoothing was applied to the 2D and 3D images (Fig. 3A) may be related to our use of

the ROI maximum pixel to measure lesion activity. The maximum pixel will tend to overestimate the underlying value in noisy images and may account for the higher target-to-background ratios found in the more noisy 2D data. As meaningful comparisons of image noise can be made only under conditions of matched spatial resolution, we chose to apply slightly less smoothing to the 3D images to reproduce the same target-to-background ratio as the 2D images. A 5-mm gaussian filter was found to give a mean target-to-background ratio that was not significantly different from that of the 2D images and all noise comparisons were thus performed under conditions of matched target-to-background ratio. The use of the slightly narrower filter for the 3D images ensured that the noise comparison was not biased in favor of 3D.

Our use of 2 iterations and 8 subsets applied uniformly to all patients for both 2D and 3D reconstructions is likely not optimal. The difference in target-to-background ratios when identical 6-mm gaussian smoothing was applied to both 2D and 3D images was, however, only 5%. This indicates that, although there is no evidence that either reconstruction was completely optimized, they had both reached similar levels of convergence. Comparing image noise under these conditions is thus reasonable and further justified by our use in the noise analysis of only the 3D images with 5-mm gaussian smoothing.

The noise advantage that was observed for 3D acquisition is attributed to the high sensitivity of the septa-out mode and the narrow coincidence timing window (6 ns) afforded by the LSO detector crystals. The energy acceptance window on this scanner was the same as that for comparable BGO systems (350–650 keV) and, because 3D has a greater scatter fraction than 2D, the 3D performance of the Accel may not be optimum. Improved 3D performance is expected from newer LSO tomographs that support a higher lower level energy discriminator and have a better counting rate performance (28).

CONCLUSION

Comparisons of 2D and 3D performance are very sensitive to the specific conditions under which the data were acquired. Counting rate, scatter, activity outside the field of view, reconstruction algorithm, and scanner characteristics all influence relative performance. In this study 2D and 3D data were compared under clinically realistic conditions and effects that may introduce bias were minimized. The mean ratio of 3D to 2D image values was 0.94 with 95% limits of agreement of 0.63–1.41. All noise comparisons were made under conditions of matched lesion target-to-background ratio as measured in patient images. A statistically significant reduction in image noise was found with 3D acquisition compared with 2D, suggesting reductions in scan duration of 33% or more are feasible. This is one of the few studies of its kind to be performed with clinical patients as opposed to phantoms using a

tomograph with LSO scintillation crystals that has support for both 2D and 3D acquisition.

ACKNOWLEDGMENTS

We thank all staff of PET/CT Imaging at White Marsh, Nottingham, MD, for data acquisition; the staff of the Paul Strickland Scanner Centre, Northwood, U.K., for the acquisition of preliminary data; and Steve Bacharach and Jinyi Qi for helpful discussions. This work was supported in part by a grant from Siemens Medical Systems.

REFERENCES

- Gambhir SS, Czernin J, Schwimmer J, et al. A tabulated summary of the FDG PET literature. *J Nucl Med.* 2001;42(suppl 5):1S–93S.
- Bailey DL, Miller MP, Spinks TJ, et al. Experience with fully 3D PET and implications for future high-resolution 3D tomographs. *Phys Med Biol.* 1998; 43:777–786.
- Brix G, Zaers J, Adam LE, et al. Performance evaluation of a whole-body PET scanner using the NEMA protocol. *J Nucl Med.* 1997;38:1614–1623.
- Cherry SR, Dahlbom M, Hoffman EJ. 3D PET using a conventional multislice tomograph without septa. *J Comput Assist Tomogr.* 1991;15:655–668.
- Sorenson JA, Phelps ME. *Physics in Nuclear Medicine.* 2nd ed. Orlando, FL: Grune and Stratton; 1987:434–451.
- Badawi RD, Marsden PK, Cronin BF, et al. Optimization of noise-equivalent count rates in 3D PET. *Phys Med Biol.* 1996;41:1755–1776.
- Cherry SR, Woods RP, Hoffman EJ, et al. Improved detection of focal cerebral blood flow changes using three-dimensional positron emission tomography. *J Cereb Blood Flow Metab.* 1993;13:630–638.
- Votaw JR, White M. Comparison of 2-dimensional and 3-dimensional cardiac ⁸²Rb PET studies. *J Nucl Med.* 2001;42:701–706.
- Knesaurek K, Machac J, Krynycky BR, et al. Comparison of 2-dimensional and 3-dimensional ⁸²Rb myocardial perfusion PET imaging. *J Nucl Med.* 2003; 44:1350–1356.
- Raylman RR, Kison PV, Wahl RL. Capabilities of two- and three-dimensional FDG-PET for detecting small lesions and lymph nodes in the upper torso: a dynamic phantom study. *Eur J Nucl Med.* 1999;26:39–45.
- Lartizien C, Kinahan PE, Comtat C. A lesion detection observer study comparing 2-dimensional versus fully 3-dimensional whole-body PET imaging protocols. *J Nucl Med.* 2004;45:714–723.
- Farquhar TH, Llacer J, Hoh CK, et al. ROC and localization ROC analyses of lesion detection in whole-body FDG PET: effects of acquisition mode, attenuation correction and reconstruction algorithm. *J Nucl Med.* 1999;40: 2043–2052.
- Lodge MA, Lowe J, Lowe GE, et al. A comparison of 2D and 3D PET images using an interleaved septa-in/septa-out acquisition protocol [abstract]. *J Nucl Med.* 2002;43(suppl):206P.
- El Fakhri G, Holdsworth C, Badawi RD, et al. Impact of acquisition geometry and patient habitus on lesion detectability in whole-body FDG-PET: a channelized hotelling observer study. *Proceedings of the IEEE Nuclear Science Symposium and Medical Imaging Conference* [CD-ROM]. Norfolk, VA: IEEE; 2002
- Karp JS. Is LSO the future of PET? Against [commentary]. *Eur J Nucl Med.* 2002;29:1525–1528.
- Nutt R. Is LSO the future of PET? For [commentary]. *Eur J Nucl Med.* 2002; 29:1523–1525.
- National Electrical Manufacturers Association. *NEMA Standards Publication NU-2 1994: Performance Measurements of Positron Emission Tomographs.* Washington, D.C.: National Electrical Manufacturers Association; 1994
- Xu M, Luk WK, Cutler PD, et al. Local threshold for segmented attenuation correction of PET imaging of the thorax. *IEEE Trans Nucl Sci.* 1994;41:1532–1537.
- Bergstrom M, Eriksson L, Bohm C, et al. Correction for scattered radiation in a ring detector positron camera by integral transformation of the projections. *J Comput Assist Tomogr.* 1983;7:42–50.
- Watson CC, Newport D, Casey M, et al. Evaluation of simulation-based scatter correction for 3-D PET cardiac imaging. *IEEE Trans Nucl Sci.* 1997;44: 90–97.
- Hudson HM, Larkin RS. Accelerated image reconstruction using ordered subsets of projection data. *IEEE Trans Med Imaging.* 1994;13:601–609.

22. Liu X, Comtat C, Michel C, et al. Comparison of 3-D reconstruction with 3D-OSEM and with FORE+OSEM for PET. *IEEE Trans Med Imaging*. 2001; 20:804–814.
23. Bland JM, Altman DG. Measuring agreement in method comparison studies. *Stat Methods Med Res*. 1999;8:135–160.
24. Bland JM, Altman DG. Statistical methods for assessing agreement between two methods of clinical measurement. *Lancet*. 1986;1:307–310.
25. Bland JM, Altman DG. Measurement error proportional to the mean. *Br Med J*. 1996;313:106.
26. Riddell C, Carson RE, Carrasquillo JA, et al. Noise reduction in oncology FDG PET images by iterative reconstruction: a quantitative assessment. *J Nucl Med*. 2001;42:1316–1323.
27. Everaert H, Vanhove C, Lahoutte T, et al. Optimal dose of ¹⁸F-FDG required for whole-body PET using a LSO PET camera. *Eur J Nucl Med Mol Imaging*. 2003;30:1615–1619.
28. Casey ME, Young J, Wheelock T, et al. Physical performance of a high resolution PET/CT scanner [abstract]. *J Nucl Med*. 2004;45(suppl): 100P.